Chapter 7

Corrosion and tribological behaviours of sintered Ti-$Co_{0.35}$-$Cr_{0.35}$-Nb-Zr, Ti-Nb-Ta-Cr-$Co_{0.2}$, and Ti-Nb-Ta-$Fe_{0.35}$-$Co_{0.35}$ HEAs in SBF

7.1. Introduction

Promising efforts have been made in the field of implants to develop materials that are least chemically active, non-irritating, non-toxic, and effectively interact with the target tissues. Implant materials during operation within the human body experience wear and friction with the surrounding tissues. Simultaneously, the corrosive environment in the human body often leads to wear accompanied by corrosion, resulting in corrosive wear. The extent of material loss due to corrosive wear frequently surpasses that caused independently by corrosion and wear. Consequently, implant alloys should exhibit high resistance to both wear and corrosion in the physiological environment. Studies have explored the interplay between wear and corrosion in simulated physiological conditions for conventional biomedical metallic materials, such as 316L, Co-Cr-Mo alloys, and Ti-based alloys [278-281]. The corrosive wear behaviour significantly impacts the long-term reliability of multi-component implant materials. Moreover, the distinctive properties of HEAs are different from those of conventional alloys, which may influence their corrosive wear behaviour and mechanisms, over extended periods. However, a comprehensive understanding of the wear and corrosive behaviours of HEAs in simulated physiological environments is required.

The present chapter focuses on the corrosion and tribological performance of the developed HEAs (i.e., Ti-$Co_{0.35}$-$Cr_{0.35}$-Nb-Zr, Ti-Nb-Ta-Cr-$Co_{0.2}$, and Ti-Nb-Ta-$Fe_{0.35}$-$Co_{0.35}$). Electrochemical methodologies such as OCP, EIS, and PDP were employed to evaluate the

corrosion resistance of the current HEAs in the presence of SBF (pH = 7.4). Extensive analysis of the alloy's surface after corrosion was conducted using FE-SEM. The tribological performance of the alloys was investigated in the presence of SBF against zirconia balls at loads of 10, 15, and 20 N. The study thoroughly discusses various wear parameters such as the coefficient of friction, width of worn surface, maximum lateral depth, wear rate, wear volume, and wear mechanisms. In-depth discussions are presented on the findings from SEM images and EDS analysis.

7.2. Materials and methodology

The methods and parameters for conducting the corrosion and wear analysis of the sintered samples in SBF have been outlined in detail in Chapter 3.

7.3. Results and discussion

7.3.1 Electrochemical analysis

This section analyses and discusses the results obtained from electrochemical testing, including OCP, EIS, and PDP tests. The OCP test was conducted to stabilize the developed sintered HEAs and Ti-6Al-4V alloy (for comparative purposes). OCP, also known as the stable potential, is the voltage difference between the electrodes of an electrochemical cell or system when no current is flowing. It represents the equilibrium voltage, indicating no net transfer of electrons or ions between the electrodes. The OCP for all the samples becomes stable within 60 minutes of testing as shown in Fig. 7.1.

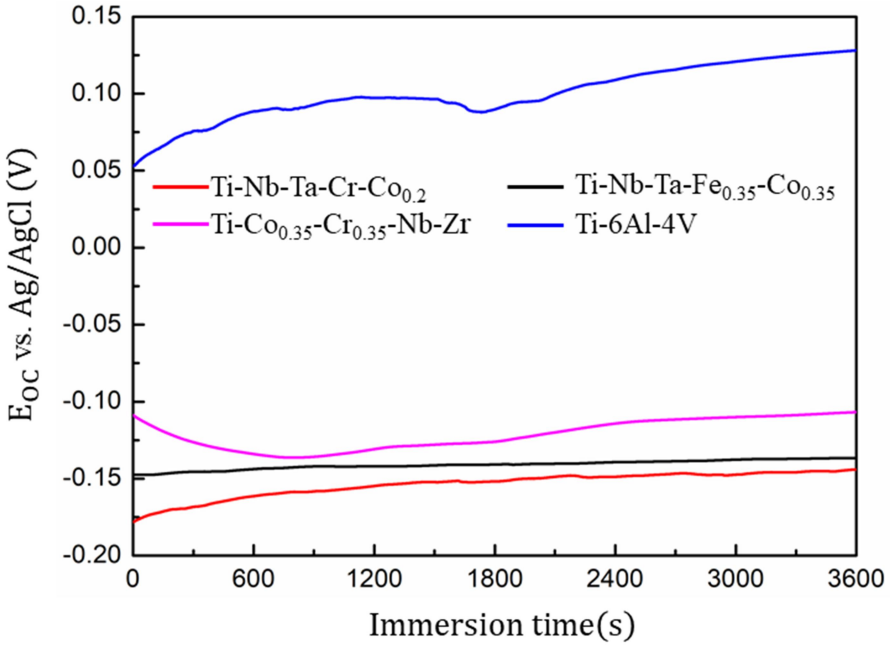

Fig. 7.1. Open circuit potential result of sintered HEAs and Ti-6Al-4V alloy in SBF.

7.3.1.1 Electrochemical impedance spectroscopic measurements

Electrochemical impedance spectroscopy is an effective technique for analyzing corrosion and passivation mechanisms, offering more detailed insights into the electrochemical reactions occurring at the surface than other electrochemical methods. Figure 7.2 shows the Nyquist plot for sintered HEAs and the Ti-6Al-4V alloy in SBF. In the Nyquist plot, a key parameter for assessing corrosion resistance is the diameter of the semicircular arc, which directly correlates with the material's corrosion behaviour [282]. A larger diameter indicates a higher corrosion resistance due to a more protective passive film. From the Nyquist plot, it can be noticed that Ti-Nb-Ta-Cr-$Co_{0.2}$ HEA has the largest semicircular arc diameter, indicating its highest corrosion resistance property, whereas the Ti-6Al-4V alloy has the smallest semicircular arc diameter, revealing its lowest corrosion resistance. The semicircular arc diameters of the other two HEAs (i.e., Ti-Nb-Ta-$Fe_{0.35}$-$Co_{0.35}$ and Ti-$Co_{0.35}$-$Cr_{0.35}$-Nb-Zr) fall between those of the Ti-Nb-Ta-Cr-$Co_{0.2}$ HEA and the Ti-6Al-4V alloy. Therefore, the

Nyquist plot demonstrates that the Ti-Nb-Ta-Cr-$Co_{0.2}$ HEA exhibits the highest corrosion resistance in SBF with a pH of 7.4, while the Ti-Nb-Ta-$Fe_{0.35}$-$Co_{0.35}$ and Ti-$Co_{0.35}$-$Cr_{0.35}$-Nb-Zr HEAs show better corrosion resistance than the Ti-6Al-4V alloy.

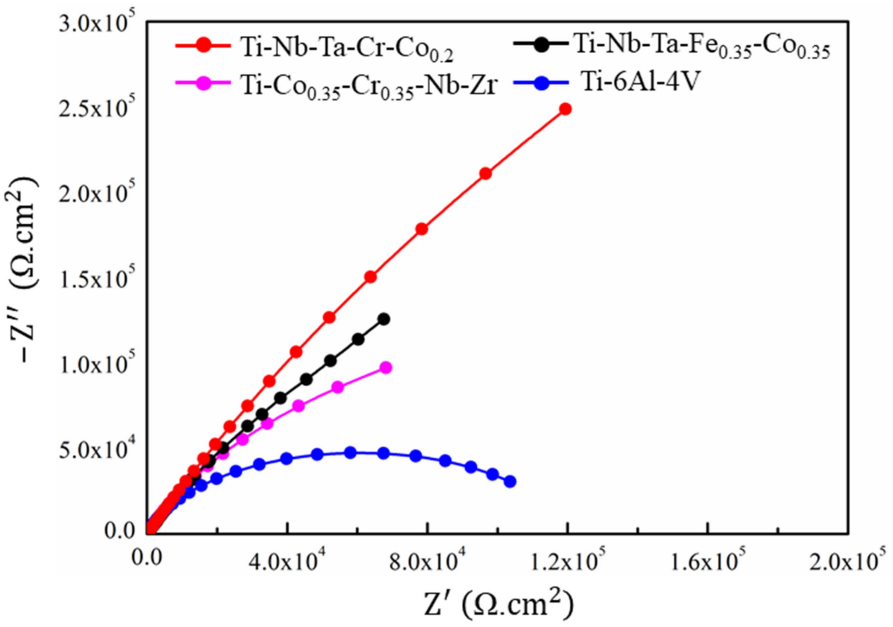

Fig. 7.2. Nyquist plots of sintered HEAs and Ti-6Al-4V alloy in SBF.

Figure 7.3 illustrates the Bode plots for sintered HEAs and the Ti-6Al-4V alloy. At higher frequencies, the impedance modulus values for sintered HEAs and the Ti-6Al-4V remain nearly constant, and the phase angle approaches zero degrees, indicating a resistor-like behaviour. This occurs because the solution resistance dominates at higher frequencies [283]. The Bode plots exhibit inclined impedance modulus and stabilized phase angle in the medium-low frequency regions. This behaviour reveals the presence of a barrier oxide film on the surface, and a capacitive response is expected [284]. As a result, the equivalent electrical circuit (Fig. 7.4) is structured around two regions. The first region represents the surface of the air-formed passive film, and the second region corresponds to the exposed areas where pits might develop around surface defects. Moreover, Ti-6Al-4V alloy displays a phase angle of -65 degrees, which is lower than the sintered HEAs (-70 to -75 degrees) in the

same frequency region, suggesting that the passive film formed in SBF is not as robust as that of sintered HEAs. It is noteworthy that the metallic states of Ti, Nb, Ta, Cr, Fe, and Zr within the passive oxide film, along with OH^- species attached to the surface, are believed to play a critical role in repairing and forming a continuous passive film. This process enhances corrosion resistance when the surface is exposed to chloride ion attacks [284, 285].

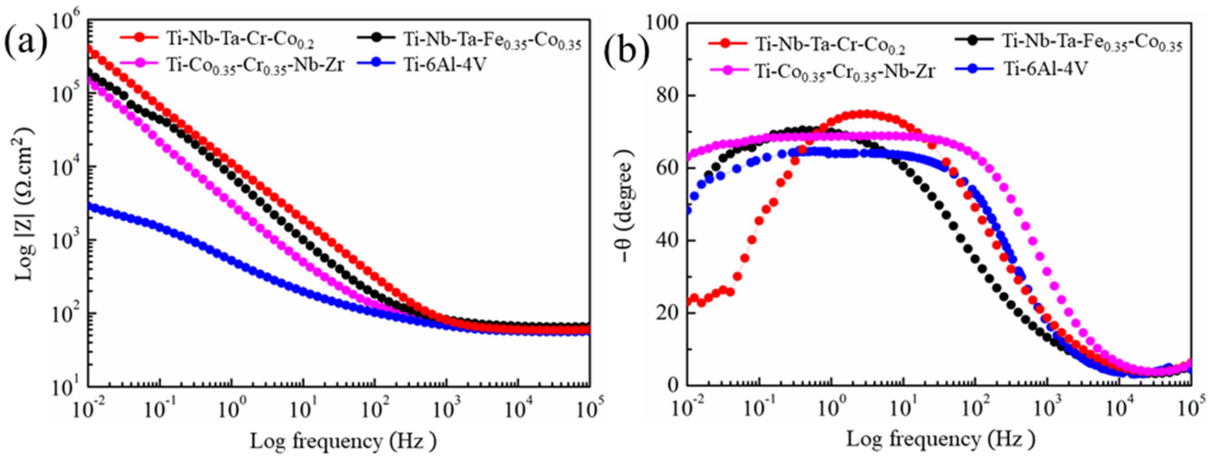

Fig. 7.3. Bode plots of sintered HEAs and Ti-6Al-4V alloy in SBF, (a) impedance spectra and (b) trends corresponding to the bode plots with respect to phase angle.

ZView® software was used to analyze the impedance characteristics using the "equivalent circuit" shown in Fig. 7.4. This method quantitatively validated the results obtained from EIS. The equivalent circuit parameters were adjusted to fit the EIS data more accurately and include R_s, CPE1, CPE2, R_1, and R_2. Here, R_s represents the solution resistance, while R_1 and R_2 correspond to the resistances of the passive film and charge transfer, respectively. CPE1 and CPE2 denote the constant phase elements (CPE) of the passivation film and the electric double layer. At solid electrodes, the double-layer capacitance does not exhibit purely capacitive behavior and typically shows a frequency distribution. Thus, CPE is often used for these electrodes [286]. Considering that real polycrystalline solid surfaces have defects,

scratches, irregularities, and a pore, R_2 is coupled with CPE2 in parallel to describe the process occurring at the exposed pit areas around surface defects [170].

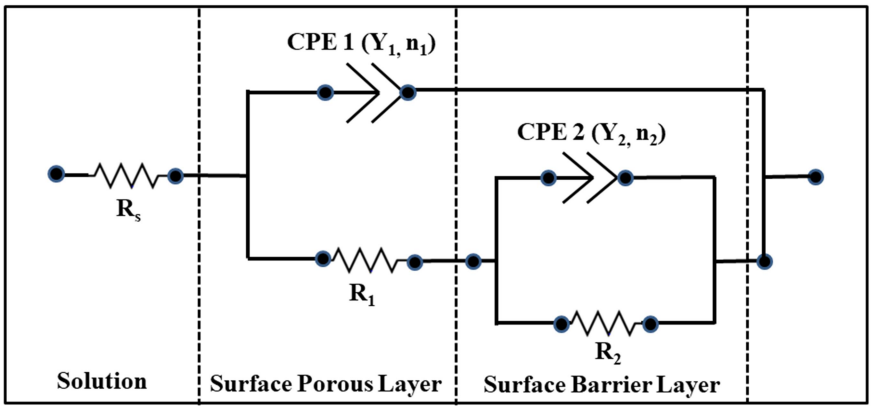

Fig. 7.4. Equivalent circuit models for fitting and simulating the impedance spectra.

Table 7.1 presents the fitting parameters derived from the EIS data that is fitted well with the equivalent circuit model. The standard deviation parameter (χ^2) indicates the accuracy of the circuit fitting. For both sintered HEAs and Ti-6Al-4V, the calculated χ^2 values, representing the percentage error of each parameter in the equivalent circuit, are of the order of magnitude 10^{-3}. This meets the mathematical fitting criterion according to Assis et al. [287], who stated that the $\chi^2 \leq 10^{-3}$.

The resistances of the outer porous layers for the Ti-Nb-Ta-Cr-$Co_{0.2}$, Ti-Nb-Ta-$Fe_{0.35}$-$Co_{0.35}$, Ti-$Co_{0.35}$-$Cr_{0.35}$-Nb-Zr, and Ti-6Al-4V alloys were determined to be 6.21 X 10^4, 5.92 X 10^4, 3.57 X 10^4, and 2.48 X $10^4 \Omega$ cm^2 respectively. Notably, the Ti-Nb-Ta-Cr-$Co_{0.2}$ alloy demonstrated the highest resistance, suggesting its outer porous layer is more corrosion-resistant than the other alloys in SBF. Conversely, the Ti-6Al-4V alloy exhibited the lowest resistance, indicating lower stability in corrosive environments. For all the samples, the resistance of the inner barrier layer (R_2) was higher than that of the outer porous layer (R_1), implying greater corrosion resistance of the inner layer. Corrosion protection is attributed to

both layers [288]. HEAs are likely to effectively reform the passive film over surface defects due to the presence of highly electronegative elements. Elements such as Nb, Ti, Fe, Co, Cr, and Ta with electronegativities of 1.60, 1.54, 1.83, 1.88, 1.66, and 1.50 respectively, can readily gain electrons [289]. Increased metal electronegativity reduces the electronegativity difference between oxygen and metal, adhering to acid-base principles, thus protecting the metal by regenerating the oxide layer and mitigating corrosion [170]. A comparison of the capacitance values CPE1 and CPE2 within the framework of the proposed equivalent circuit revealed that the capacitance associated with the inner barrier layer (CPE2) was consistently lower than that of the outer layer (CPE1). Previous studies have indicated that lower capacitance values are associated with a thicker protective barrier [287, 290, 291].

Furthermore, Table 7.1 indicates that the n values lie between 0.73 and 0.92, revealing that the metal dissolution is governed by a mixed process [292]. Specifically, n represents the coefficient of diffusion that lies between $-1 \leq n \leq 1$. Here, $n = -1$ corresponds to a pure inductance, $n = 0$ represents an ideal resistance, and $n = 1$ reveals pure capacitance.

Table 7.1 Equivalent circuit elements values obtained by fitting the experimental result of EIS in SBF solution

Sample	R_s	R_1	CPE_1		R_2	CPE_2		χ^2
	(Ω cm^2)	X 10^4 (Ω cm^2)	Y_1 X 10^{-6} (Ω^{-1} cm^{-2} s^{n_1})	n_1	X 10^4 (Ω cm^2)	Y_2 X 10^{-6} (Ω^{-1} cm^{-2} s^{n_2})	n_2	X 10^{-3}
A	58.47	6.21	28.34	0.87	111.72	16.23	0.91	2.751
B	57.91	5.92	31.76	0.81	94.51	22.81	0.88	1.343
C	57.12	3.57	38.45	0.89	57.13	31.53	0.73	0.967
D	58.93	2.48	53.62	0.92	44.62	39.14	0.79	0.536

(A)- Ti-Nb-Ta-Cr-$Co_{0.2}$ (**B)-**Ti-Nb-Ta-$Fe_{0.35}$-$Co_{0.35}$ **(C)-** Ti-$Co_{0.35}$-$Cr_{0.35}$-Nb-Zr

(**D)-**Ti-6Al-4V

7.3.1.2 Potentiodynamic polarization behaviour

Figure 7.5 illustrates the potentiodynamic polarization behaviour of sintered HEAs and the Ti-6Al-4V alloy in SBF (pH = 7.4). By extrapolating the Tafel curve, the anodic and cathodic slopes were used to calculate the corrosion current density (I_{corr}) and corrosion potential (E_{corr}). The point of intersection of cathodic and anodic slopes decides the values of I_{corr} and E_{corr}. The Tafel plot is used to calculate the corrosion rate (C_R). The sintered HEAs contain a large passive zone, indicating that the alloy has the potential to passivate. The electrochemical properties related to basic corrosion behaviour, such as E_{corr}, I_{corr}, and C_R for both sintered HEAs and the Ti-6Al-4V alloy in SBF, are presented in Table 7.2. The corrosion potential of Ti-Nb-Ta-Cr-$Co_{0.2}$, Ti-Nb-Ta-$Fe_{0.35}$-$Co_{0.35}$, Ti-$Co_{0.35}$-$Cr_{0.35}$-Nb-Zr, and Ti-6Al-4V alloys were determined to be 0.1324, 0.0415, -0.1399, and -0.2324 V, respectively. However, the corresponding corrosion current density values were 1.177 X 10^{-7}, 1.554 X 10^{-7}, 1.743 X 10^{-7}, and 3.423 X 10^{-7} A/cm^2, respectively. From a thermodynamic

viewpoint, a higher E_{corr} indicates greater corrosion resistance. It can be observed that the corrosion potential is highest for Ti-Nb-Ta-Cr-$Co_{0.2}$ HEA and lowest for Ti-6Al-4V alloy. Typically, I_{corr} is a critical parameter for assessing the corrosion rate and the kinetics of corrosion processes at the corrosion potential. As per the ASTM G102-89 standard [293], the C_R (in mm/year) can be calculated using Eq. (7.1).

$$C_R = \frac{KI_{corr}E_w}{\rho}\left(\frac{mm}{yr}\right) \tag{7.1}$$

Where, K = 3272 (mm A^{-1} cm^{-1} yr^{-1}), E_w = equivalent weight of samples (g eq^{-1}), I_{corr} = corrosion current density (μA cm^{-2}), and ρ = density of alloys (g cm^{-3}), respectively. The corrosion rate is directly proportional to the corrosion current density of the alloy [294, 295]. The corrosion current density is lowest for Ti-Nb-Ta-Cr-$Co_{0.2}$ HEA, revealing better corrosion-resistant properties, whereas Ti-6Al-4V alloy shows the highest corrosion current density, revealing less corrosion-resistant material in SBF. The other two HEAs (i.e., Ti-Nb-Ta-$Fe_{0.35}$-$Co_{0.35}$ and Ti-$Co_{0.35}$-$Cr_{0.35}$-Nb-Zr) show better résistance towards corrosion than Ti-6Al-4V.

Almost all metals and their alloys form a protective oxide layer on their surface when exposed to a corrosive environment. When an alloy surface containing Ti, Zr, Nb, Ta, Cr, and Fe is exposed to a corrosive environment, the passive films developed on the surface are mainly composed of TiO_2, Nb_2O_5, ZrO_2, Ta_2O_5, Fe_2O_3, and Cr_2O_3, respectively [9, 164, 170, 296]. This oxide layer acts as a barrier, protecting the material from corrosion and thus making it more corrosion-resistant. The oxide layers exhibit different morphologies based on the base metal and the oxide-forming element, which significantly influences the inward flow of oxygen and the development of a protective oxide layer on the surface [297]. For example, a triplex oxide scale on Fe-19Cr-9Ni stainless steel consists of an outer layer of Fe_3O_4, a thin

inner oxide layer, and an internal oxidation zone [298]. In the case of Ti, the oxide layer also comprises three distinct layers: a TiO film adjacent to the metal, a Ti_2O_3 film above it, and an outermost TiO_2 layer that interfaces with the solution [299]. When Ti is sintered with Zr, two primary oxide layers form: an outer porous layer and an inner barrier layer composed mainly of ZrO_2 and TiO_2 [300].

The corrosion rates of developed Ti-Nb-Ta-Cr-$Co_{0.2}$, Ti-Nb-Ta-$Fe_{0.35}$-$Co_{0.35}$, Ti-$Co_{0.35}$-$Cr_{0.35}$-Nb-Zr HEAs were determined to be 7.401 X 10^{-4}, 9.754 X 10^{-4}, and 1.440 X 10^{-3} mm/year, respectively, which are lower than the corrosion rate of Ti-6Al-4V alloy (2.961 X 10^{-3} mm/year). Hence, the developed HEAs can be used as a hard tissue replacement because of their lower corrosion rate in the presence of SBF than Ti-6Al-4V alloy. Hawajreh et al. [301] explored the corrosion resistance of three porous HEAs with the composition $Ti_{(25+x)}$-Nb_{25}-Zr_{25}-$Ta_{(25-x)}$ (x = 0, 5, 10 at.%), focusing on how varying the Ti/Ta ratio affects this property. The study revealed that both the corrosion rate and the release of metal ions increase with higher Ti content. Further, they have reported that the released amounts of Ti, Nb, Zr, and Ta (Ti: 2.5–5.4; Nb: 3.6–9.3; Zr: 0.6–2.5; and Ta: 0.6–6.2 $ngL^{-1}\,cm^{-2}\,h^{-1}$) remained below reported toxic levels for animal/human health.

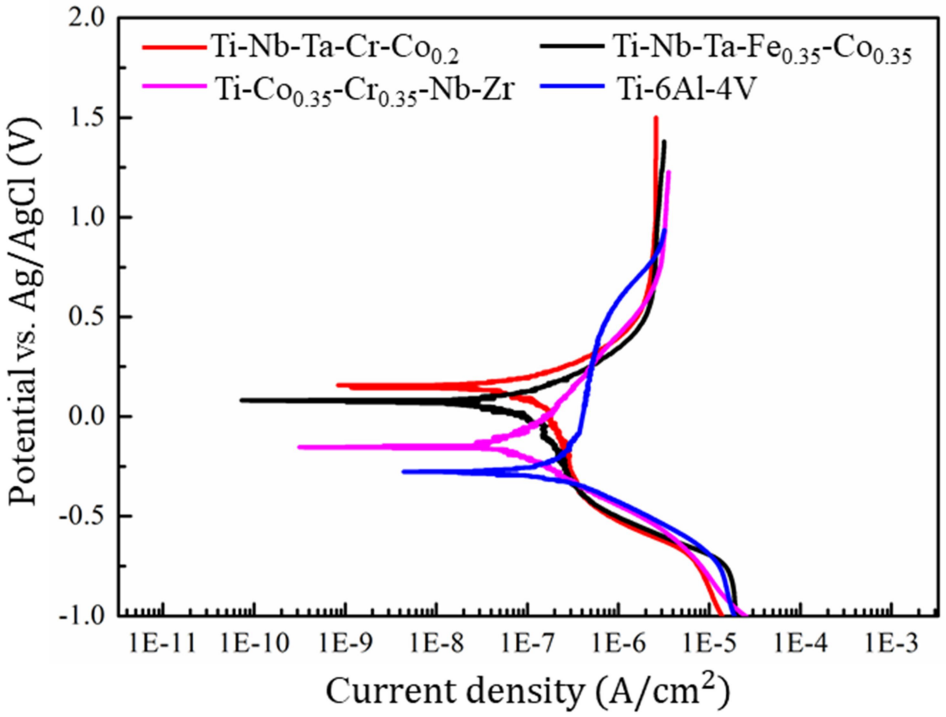

Fig. 7.5. Potentiodynamic polarization curve of sintered HEAs and Ti-6Al-4V alloy in SBF.

Table 7.2 Corrosion parameters of the sintered samples obtained from potentiodynamic polarization curves in the presence of SBF solution

Sample	**Corrosion potential** E_{corr} (V)	**Corrosion current density** I_{corr} (A/cm^2)	**Corrosion rate** (mm/year)
Ti-Nb-Ta-Cr-$Co_{0.2}$	0.1324	1.177×10^{-7}	7.401×10^{-4}
Ti-Nb-Ta-$Fe_{0.35}$-$Co_{0.35}$	0.0415	1.554×10^{-7}	9.754×10^{-4}
Ti-$Co_{0.35}$-$Cr_{0.35}$-Nb-Zr	-0.1399	1.743×10^{-7}	1.440×10^{-3}
Ti-6Al-4V	-0.2324	3.423×10^{-7}	2.961×10^{-3}

7.3.1.3 Corroded surface investigation

After the corrosion tests, the surface morphology of the corroded samples was examined using FE-SEM to observe the initiation of pits, as depicted in Fig. 7.6. The FE-SEM images indicate that the sintered HEAs exhibit nano-sized pits that are fewer in number compared to the Ti-6Al-4V alloy, which displays macro-pits. This microstructure suggests that the corrosion occurs via a pitting corrosion mechanism. Additionally, the size and number of pits vary among the sintered HEAs. Specifically, the Ti-Nb-Ta-Cr-$Co_{0.2}$ HEA shows relatively smaller and fewer pits compared to the Ti-Nb-Ta-$Fe_{0.35}$-$Co_{0.35}$ and Ti-$Co_{0.35}$-$Cr_{0.35}$-Nb-Zr HEAs. The EIS and PDP results are in agreement with the FE-SEM images of the corroded samples.

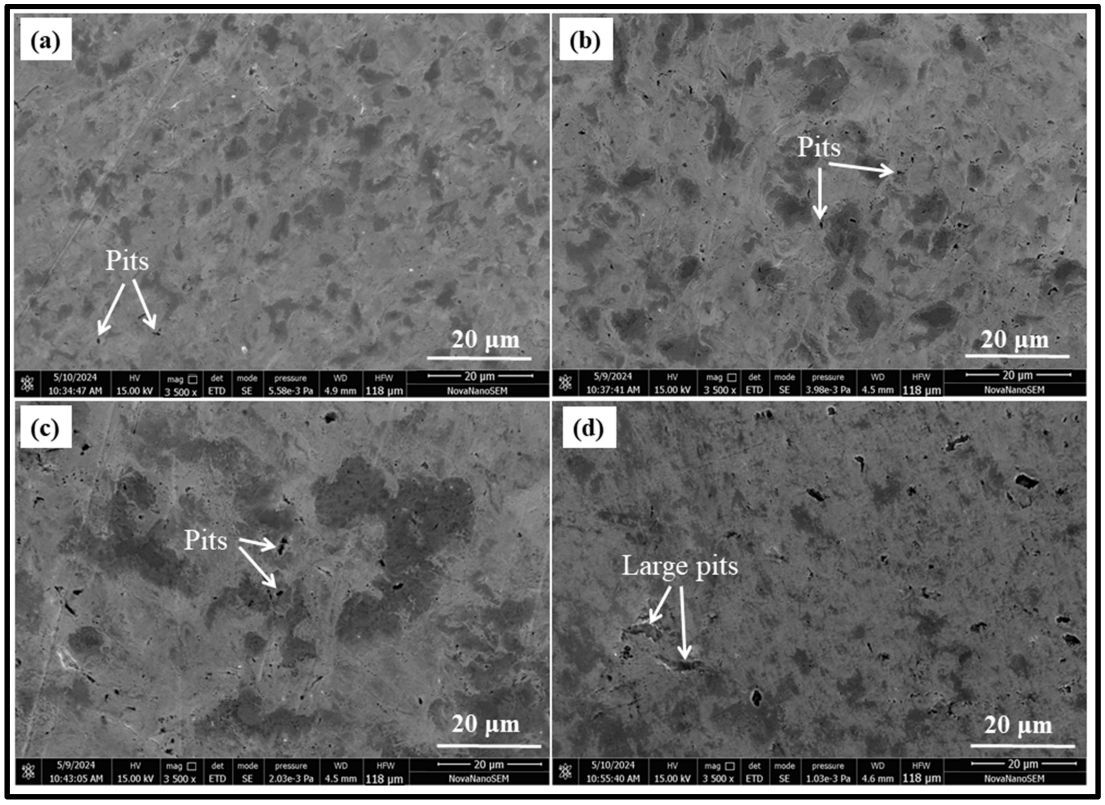

Fig. 7.6. FE-SEM images of the corroded samples, (a) Ti-Nb-Ta-Cr-$Co_{0.2}$, (b) Ti-Nb-Ta-$Fe_{0.35}$-$Co_{0.35}$, (c) Ti-$Co_{0.35}$-$Cr_{0.35}$-Nb-Zr, and (d) Ti-6Al-4V.

7.3.2 Wear and frictional behaviour of alloys

7.3.2.1 Coefficient of friction value

Figure 7.7 illustrates the coefficient of friction (COF) vs. running cycle for Ti-Nb-Ta-Cr-$Co_{0.2}$, Ti-Nb-Ta-$Fe_{0.35}$-$Co_{0.35}$, Ti-$Co_{0.35}$-$Cr_{0.35}$-Nb-Zr, and Ti-6Al-4V alloys under loads of 10, 15, and 20 N, respectively. In Fig. 7.7(a), Ti-Nb-Ta-Cr-$Co_{0.2}$HEA at a 10 N load reaches a maximum COF of 0.62 shortly after the test begins, stabilizing after 2000 cycles. A similar trend was observed at a 15 N load, with the maximum COF slightly exceeding that of the 10 N load. At a 20 N load, the maximum COF was 0.48 at the beginning and became stable after 800 cycles. Over the 7200 cycles, the average COF values for the 10 N, 15 N, and 20 N loads were 0.515 ± 0.02, 0.463 ± 0.03, and 0.402 ± 0.04, respectively.

The Ti-Nb-Ta-$Fe_{0.35}$-$Co_{0.35}$, Ti-$Co_{0.35}$-$Cr_{0.35}$-Nb-Zr, and Ti-6Al-4V alloys exhibited a similar trend where the COF reached a maximum value at different loads before stabilizing after a certain number of running cycles. Figure 7.7(b-d) reveals different numbers of cycles for the alloys at different loads to attain the steady-state friction coefficient values. The average COF values for Ti-Nb-Ta-$Fe_{0.35}$-$Co_{0.35}$, Ti-$Co_{0.35}$-$Cr_{0.35}$-Nb-Zr, and Ti-6Al-4Valloys at 10 N loads were 0.585 ± 0.01, 0.625 ± 0.02, and 0.332 ± 0.04, respectively. At 15 N loads, the values were 0.504 ± 0.04, 0.512 ± 0.03, and 0.288 ± 0.02, respectively. At 20 N loads, the values were 0.443 ± 0.02, 0.459 ± 0.03, and 0.272 ± 0.02, respectively (Fig. 7.8). Thus, Ti-$Co_{0.35}$-$Cr_{0.35}$-Nb-Zr HEA is showing the highest COF and Ti-6Al-4V is showing the minimum COF at all the loading conditions.

The friction coefficient is influenced by the load magnitude, surface condition, and the relative hardness of the interacting parts [302]. As shown in Fig. 7.7(a-d), an increase in load leads to a decrease in the average COF. Initially, the alloy structure undergoes slight compression under the applied load. This initial compression stage is marked by minor

deformations in the materials microstructure. As the load increases, the pressure at the contact points causes particles to gradually detach from the alloy's surface. This detachment process begins at the microscopic level and becomes more pronounced as the load intensifies. As more particles are dislodged, they accumulate at the interface between the counter ball and the sample. These dislodged particles, often referred to as wear debris [303]. Instead of direct metal-to-metal contact, the interaction now includes a layer of loose particles. These wear debris particles act as a solid lubricant. They reduce the direct contact area between the mating surfaces and facilitate smoother sliding motion, lowering COF. Thus, the observed decrease in the average COF with increasing load can be attributed to the dual effect of initial structural compression and the formation of a lubricating layer of wear debris.

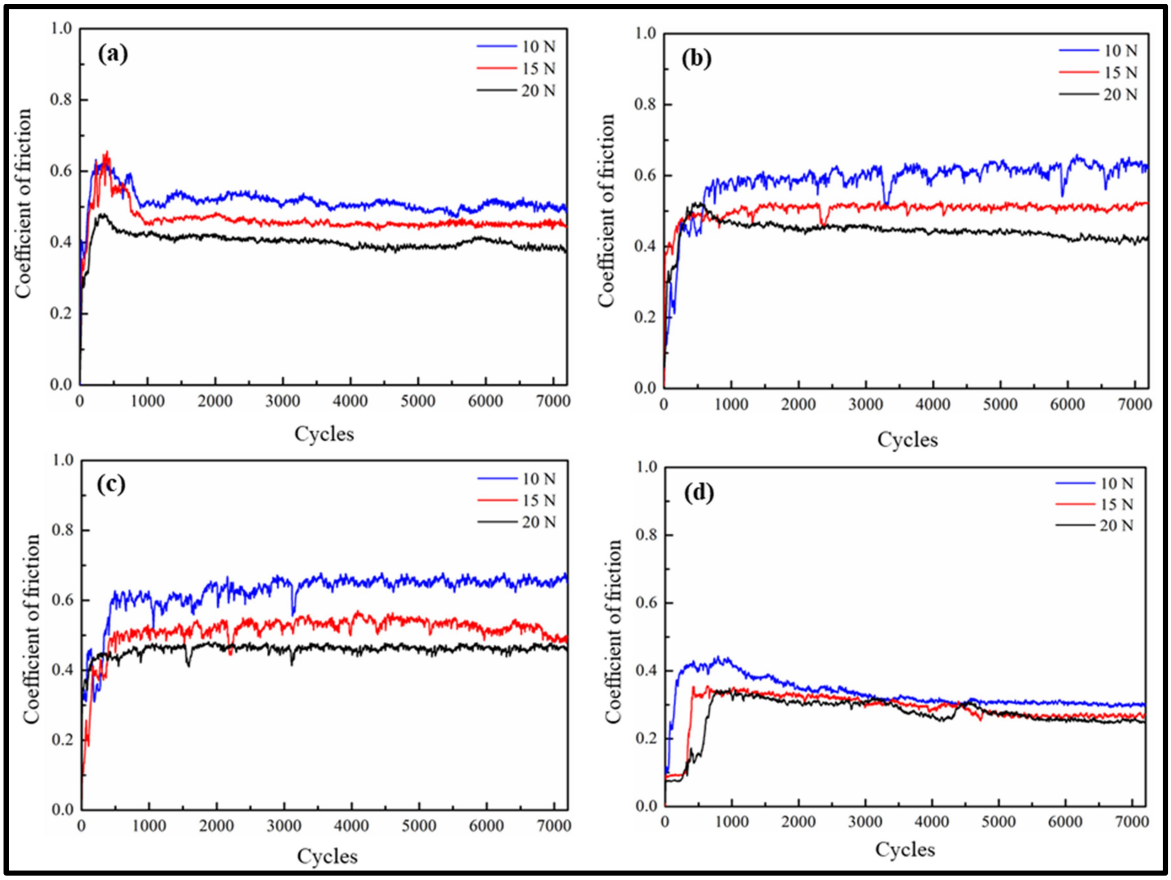

Fig. 7.7. Coefficient of friction vs. running cycles graph for 7200 cycles of samples, (a) Ti-Nb-Ta-Cr-$Co_{0.2}$, (b) Ti-Nb-Ta-$Fe_{0.35}$-$Co_{0.35}$, (c) Ti-$Co_{0.35}$-$Cr_{0.35}$-Nb-Zr, and (d) Ti-6Al-4V at 10, 15, and 20 N loads, respectively.

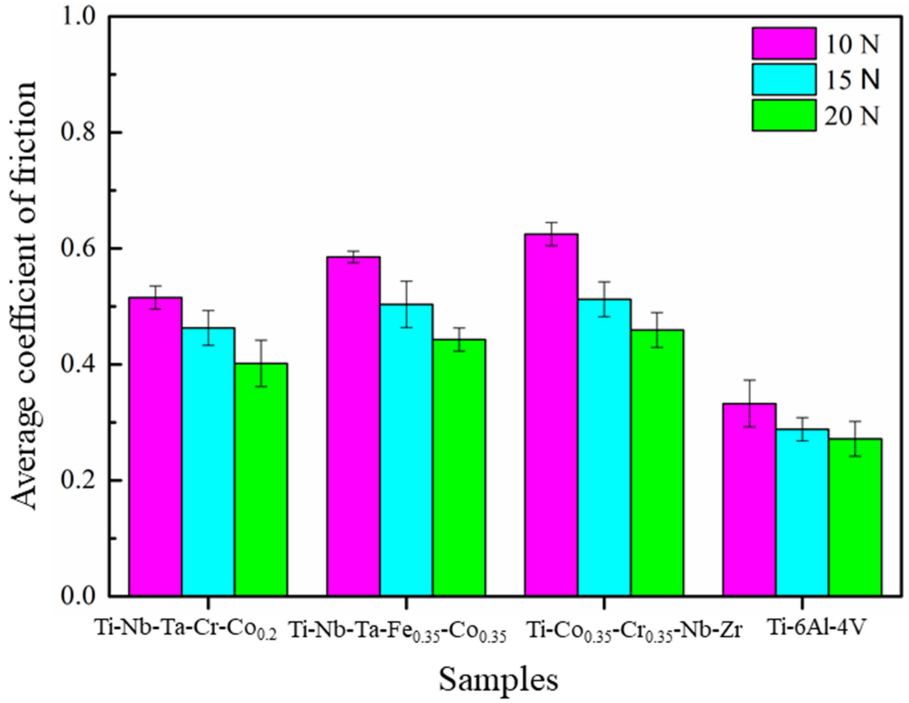

Fig. 7.8. Average friction coefficient of samples running after 7200 cycles at 10, 15, and 20 N loads, respectively.

7.3.2.2 Wear volume and wear rate

To calculate the volumetric wear and wear rate of the worn surfaces, a profilometer is used to generate the 2D profile of the worn surfaces. Figure 7.9 shows the area, width, and maximum depth of the worn surfaces at 10, 15, and 20N loads, respectively. Figure 7.9 reveals that with the increase in loading, the scar width and depth of the worn surfaces for all the samples increases. The width and depth of the worn surface mainly depend upon the microstructure, density, hardness, and elastic modulus of the developed alloys. Iijima et al. [304] reported that the hardness of the counter material also affects the wear depth of the worn surfaces. Among all the tested samples, Ti-Nb-Ta-Cr-$Co_{0.2}$ HEA has the maximum hardness while Ti-6Al-4V has the minimum. Figure 7.10 shows the maximum depth of worn surfaces of all the samples at 10, 15, and 20 N loading, respectively. Ti-Nb-Ta-Cr-$Co_{0.2}$ HEA shows the

minimum scar width and depth of the worn surfaces, while the maximum is by Ti-6Al-4V alloy at all loading conditions.

The wear volume loss (ΔV) and wear rate (W_v) of the worn surfaces are calculated using Eqs. (3.5 - 3.7) (chapter 3), for all the samples. The results obtained after the wear test of the samples in the presence of SBF are summarized in Table 7.3. The wear rate varies with sample compositions and loading conditions, as shown in Fig. 7.11. It can be noticed from Table 7.3 that as the load increases, the wear rate increases. All the worn samples have shown the same trend. Ti-Nb-Ta-Cr-$Co_{0.2}$ HEA has a minimum wear rate of 4.44 X 10^{-8} (mm^3/mm) at 10 N of loading, while Ti-6Al-4V has the maximum wear compared to developed HEAs at all loading conditions. Ti-6Al-4V has shown the minimum COF, but at the same time, it is also showing the maximum wear rate. Hence, other than lower COF, the wear rate also depends on the surface mechanical properties such as hardness, elastic modulus, Hertzian contact pressure, and the loading magnitude. The COF indicates the lubrication effectiveness of the contact surface, while the wear rate measures the extent of material degradation. Consequently, a high friction coefficient does not necessarily correlate with a high wear rate. Wang et al. [9] fabricated Ti-Zr-Hf-Nb-Fe HEA by varying the concentration of Fe. They reported that the alloy with the highest friction coefficient shows the lowest wear rate among all the developed alloys. They further noted that this may be due to its high hardness and brittleness, which makes the surface easily damaged and generates more abrasive chips during sliding.

According to the Archard-wear model [305], wear resistance strongly correlates with hardness: the higher the hardness, the better the wear resistance. The obtained wear resistance property of the developed HEAs aligns with Archard's model. Some Ti alloys and cp-Ti, widely used as traditional biomedical materials, often suffer from "particle diseases" due to

their inadequate wear resistance once implanted in the human body. Consequently, excellent wear resistance is a crucial performance indicator for biomedical materials. Hence, from Table 7.3, it can be noticed that the developed HEAs have shown a smaller wear rate than commonly used Ti-6Al-4V implant material, which can reduce the risk of "particle disease" caused by wear debris. As a result, the developed HEAs can be seen as a promising option for orthopedic implant materials.

For the sintered HEAs samples, the calculated H/E and H^3/E^2 ratio using the *H* and *E* values obtained from the instrument hardness tester are given in Table 7.4. For comparison, the H/E and H^3/E^2 ratio values of commonly used implant materials such as 316 L SS, Co-Cr-Mo, and Ti-6Al-4V have also been reported obtained from the literature [170]. Since the mechanical performance of implant surfaces against the rubbing action of counterparts (e.g., in knee and hip joints) is critical, H/E and H^3/E^2 ratios are useful for assessing and predicting the lifetime and wear resistance of materials [170]. The H/E ratio indicates elastic strain to failure, while the H^3/E^2 ratio reflects a material resistance to plastic deformation under contact load. In other words, a higher H/E ratio signifies better elastic recovery from deformation caused by external load, and a higher H^3/E^2 ratio indicates superior resistance to plastic deformation under load. For the current developed HEAs, the experimental results (Table 7.4) shows that the H/E and H^3/E^2 ratios values are higher than that of 316L SS, Co-Cr-Mo, and Ti-6Al-4V alloys, suggesting better wear resistance. The higher H/E and H^3/E^2 ratios of the HEA samples compared to 316L SS, Co-Cr-Mo, and Ti-6Al-4V alloys can be attributed to their lower elastic modulus (*E*) and moderate hardness (*H*) values.

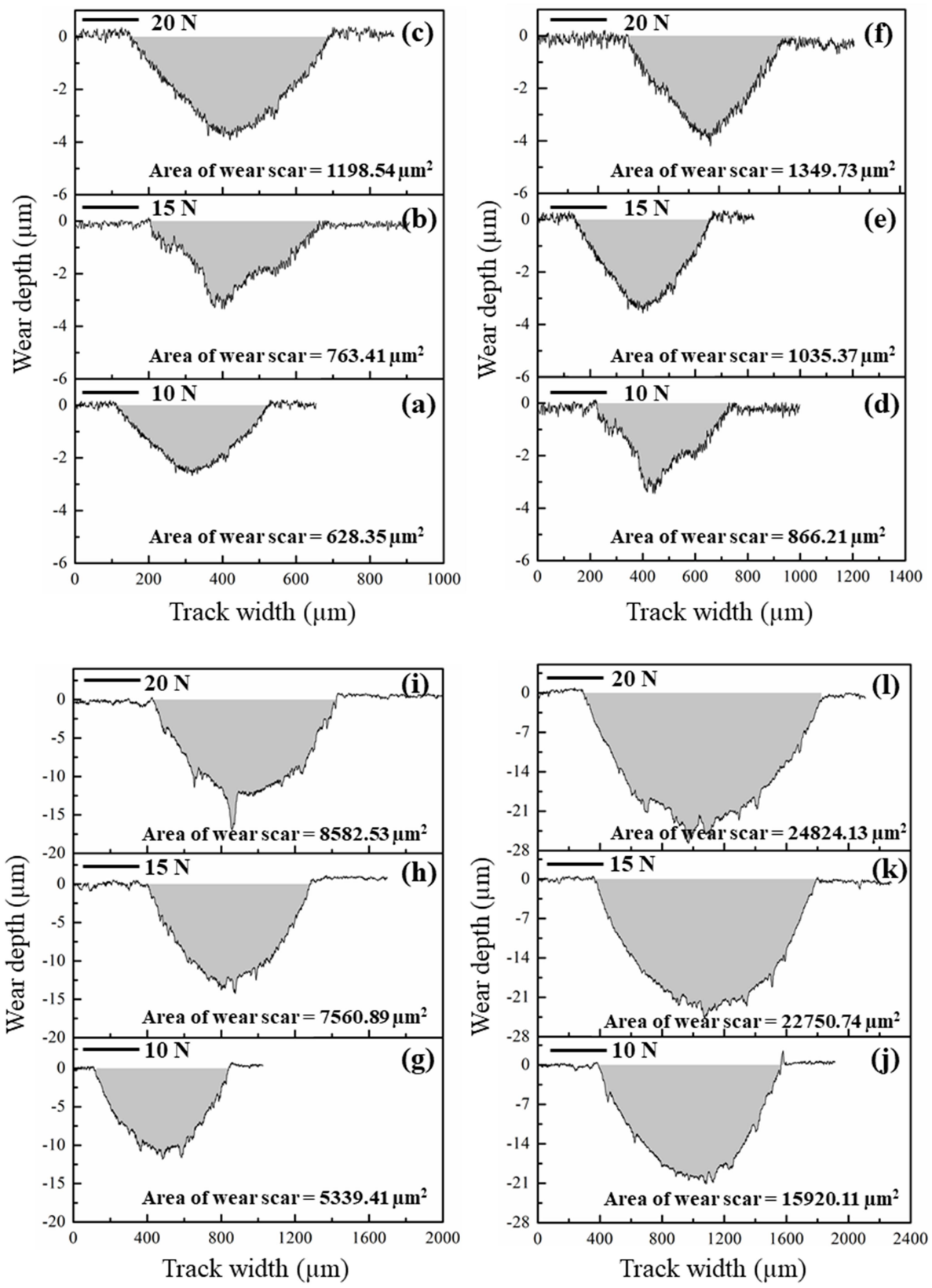

Fig. 7.9. Measurement of the worn surface by profilometer, (a, b, and c) Ti-Nb-Ta-Cr-$Co_{0.2}$, (d, e, and f) Ti-Nb-Ta-$Fe_{0.35}$-$Co_{0.35}$, (g, h, and i) Ti-$Co_{0.35}$-$Cr_{0.35}$-Nb-Zr, and (j, k, and l) of Ti-6Al-4V at 10N, 15N, and 20N load, respectively.

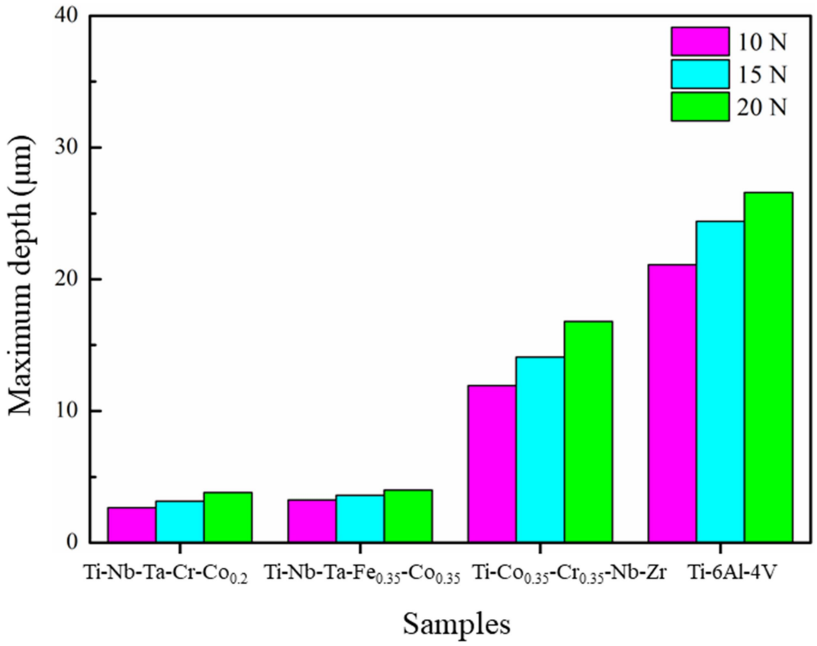

Fig. 7.10. Maximum depth of worn surfaces at 10, 15, and 20 N loading, respectively.

Table 7.3 Parameter and results obtained after wear test of the samples in SBF solution

Sample	Load (N)	Wear scar width (µm)	Wear scar cross-sectional area (μm^2)	Average depth of wear scar (µm)	Volumetric wear X 10^{-3} (mm^3)	Wear rate X 10^{-8} (mm^3/mm)
Ti-Nb-Ta-Cr-$Co_{0.2}$	10	417	628.35	1.50	1.92	4.44
	15	467	763.41	1.63	2.33	5.39
	20	550	1198.54	2.18	3.67	8.49
Ti-Nb-Ta-$Fe_{0.35}$-$Co_{0.35}$	10	525	866.21	1.65	2.64	6.11
	15	552	1035.37	1.87	3.16	7.32
	20	622	1349.73	2.17	4.12	9.54
Ti-$Co_{0.35}$-$Cr_{0.35}$-Nb-Zr	10	730	5339.41	7.31	16.85	39.02
	15	903	7560.89	8.37	23.78	55.05
	20	1008	8582.53	8.51	26.88	62.23
Ti-6Al-4V	10	1205	15920.11	13.21	50.49	116.89
	15	1431	22750.74	15.89	72.21	167.17
	20	1552	24824.13	15.99	78.48	181.68

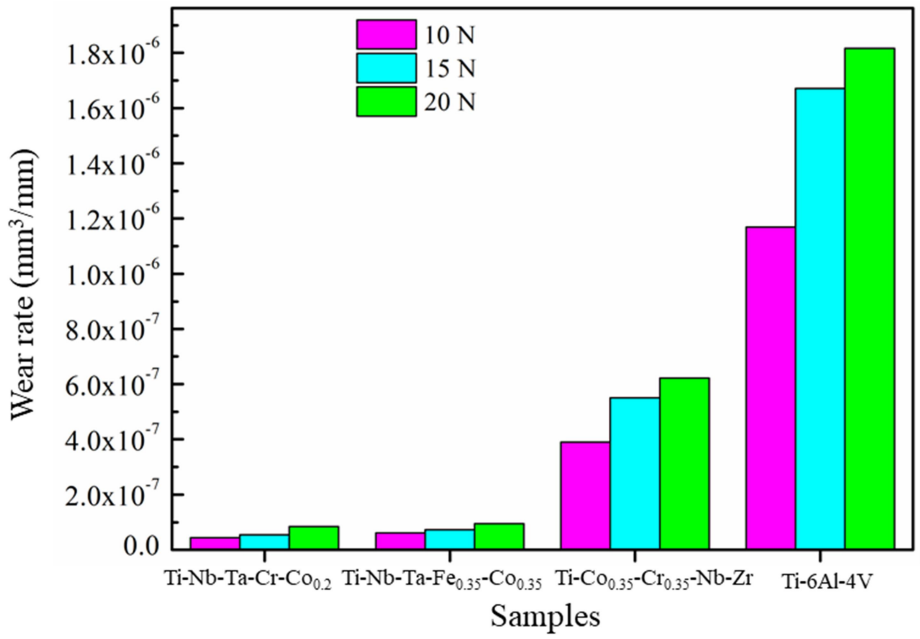

Fig. 7.11. Wear rate of all samples running after 7200 cycles against zirconia ball in SBF.

Table 7.4 Mechanical parameters measured using instrumented hardness tester [170]

	H (GPa)	E (GPa)	H/E	H^3/E^2 (GPa)
316 L SS	2.44 ± 0.18	195.62 ± 9.32	0.012	0.00038
Co-Cr-Mo	4.21 ± 0.15	222.72 ± 6.70	0.019	0.0015
Ti-6Al-4V	3.32 ± 0.15	128.20 ± 8.14	0.026	0.0022
$Ti\text{-}Co_{0.35}\text{-}Cr_{0.35}\text{-}Nb\text{-}Zr$	5.11 ± 0.4	61 ± 5	0.084	0.0358
$Ti\text{-}Nb\text{-}Ta\text{-}Cr\text{-}Co_{0.2}$	5.91 ± 0.6	82 ± 5	0.072	0.0307
$Ti\text{-}Nb\text{-}Ta\text{-}Fe_{0.35}\text{-}Co_{0.35}$	5.37 ± 0.5	73 ± 6	0.073	0.0290

7.3.2.3 Worn surface morphology

Figures. 7.12, 7.13, 7.14, and 7.15 shows the SEM images and EDS analysis of the worn surfaces of Ti-Nb-Ta-Cr-$Co_{0.2}$, Ti-Nb-Ta-$Fe_{0.35}$-$Co_{0.35}$, Ti-$Co_{0.35}$-$Cr_{0.35}$-Nb-Zr, and Ti-6Al-4V alloys at three loading conditions (10, 15, 20 N) respectively. The width of the worn surface for all the tested alloys follows the loading condition and increases with increasing load. EDS analysis of the tested alloys reveals the presence of oxygen on the wear worn surfaces. The presence of oxygen confirms the formation of an oxide layer on the alloy's surface. This oxide layer can act as a protective barrier, reducing direct metal-to-metal contact and thus increasing the wear resistance. During reciprocating friction, the continuous plastic deformation of the material can be inhibited, which initiates a sluggish effect on the wear of the materials to some extent. As a result, the wear resistance of the HEAs is enhanced [306]. The wear mechanism of Ti-Nb-Ta-Cr-$Co_{0.2}$ HEA shows adhesion, oxidation, and delamination (Fig. 7.12). It does not show the presence of any wear debris, and thus, it forms stable oxide layers on the surfaces. The wear-worn surfaces of Ti-Nb-Ta-$Fe_{0.35}$-$Co_{0.35}$ and Ti-$Co_{0.35}$-$Cr_{0.35}$-Nb-Zr HEAs show adhesion, oxidation, delamination, and loose wear debris. (Figs. 7.13 and 7.14). The absence of wear debris in Ti-Nb-Ta-Cr-$Co_{0.2}$ HEA indicates that it is more wear-resistant than Ti-Nb-Ta-$Fe_{0.35}$-$Co_{0.35}$and Ti-$Co_{0.35}$-$Cr_{0.35}$-Nb-Zr HEAs, which might be due to its higher hardness and more stable oxide formation. The wear analysis of Ti-6Al-4V is also examined for comparison purposes. The wear-worn surfaces of Ti-6Al-4V alloy show adhesion, oxidation, delamination, abrasion and wear debris (Fig. 7.15). The presence of significant abrasion and delamination shows its lower wear-resistant property, likely due to its lower hardness and the formation of less protective oxide layers on the surfaces in SBF. The wear mechanism results align with those obtained from the calculative approach. The developed HEAs show better wear resistance than Ti-6Al-4V and can be used as a future implant material.

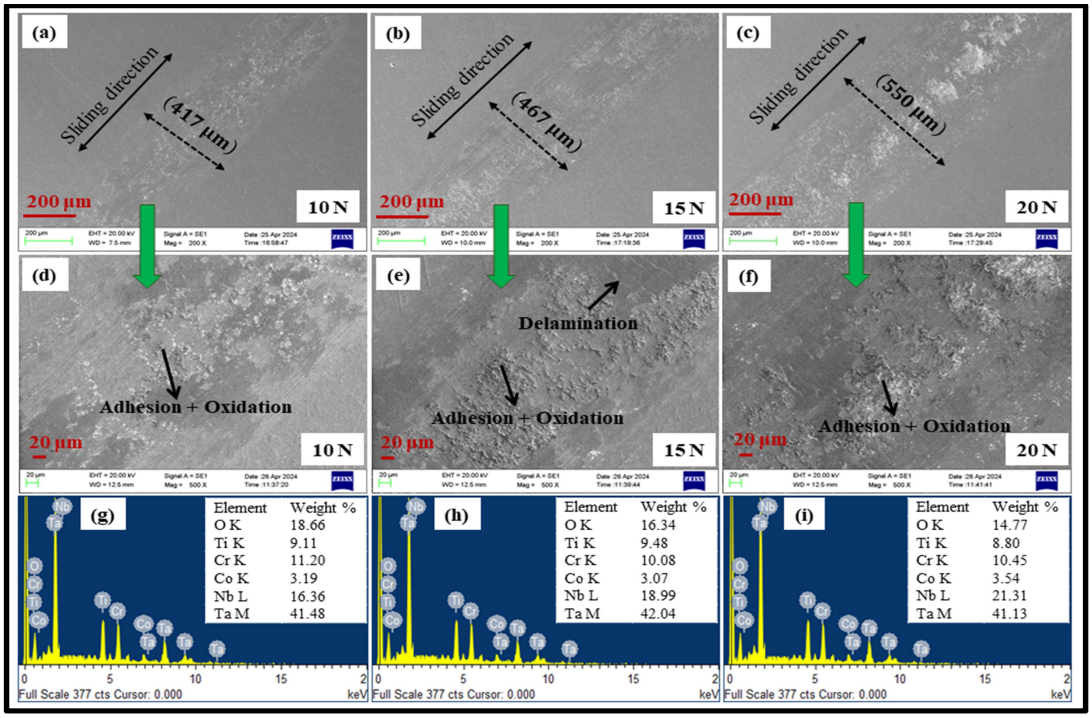

Fig. 7.12. SEM images and EDS analysis of the worn surface of Ti-Nb-Ta-Cr-$Co_{0.2}$ sample at 10 N (a, d, g), 15 N (b, e, h), and 20 N (c, f, i) load after 7200 cycles in SBF.

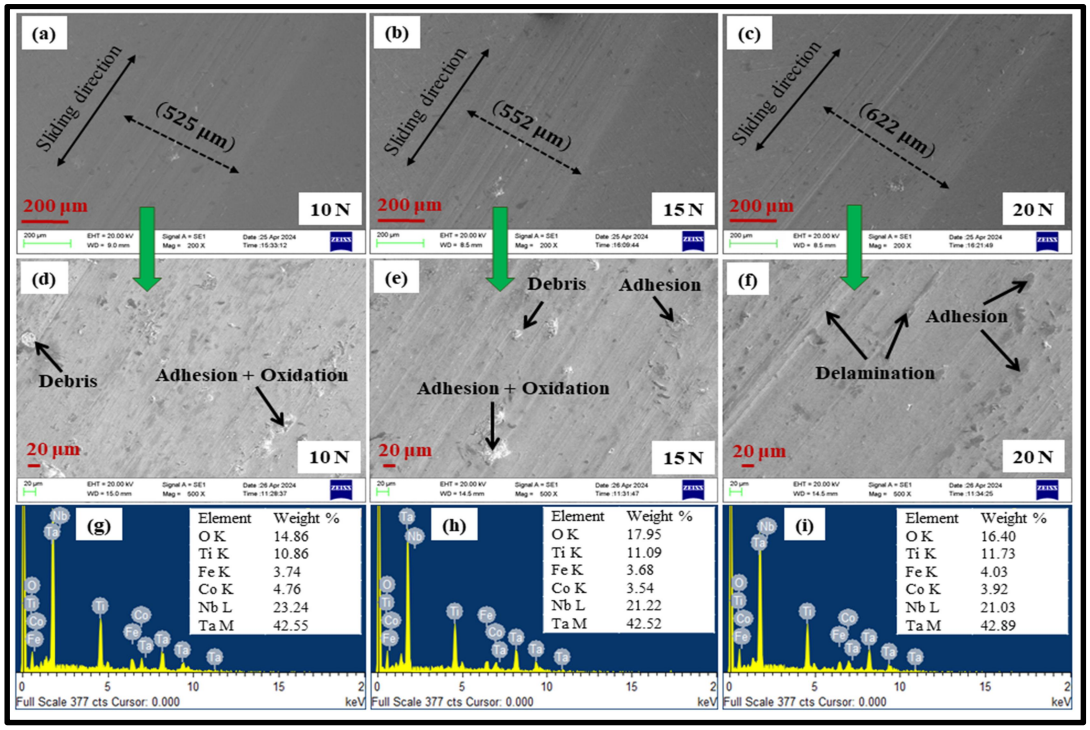

Fig. 7.13. SEM images and EDS analysis of the worn surface of Ti-Nb-Ta-$Fe_{0.35}$-$Co_{0.35}$ sample at 10 N (a, d, g), 15 N (b, e, h), and 20 N (c, f, i) load after 7200 cycles in SBF.

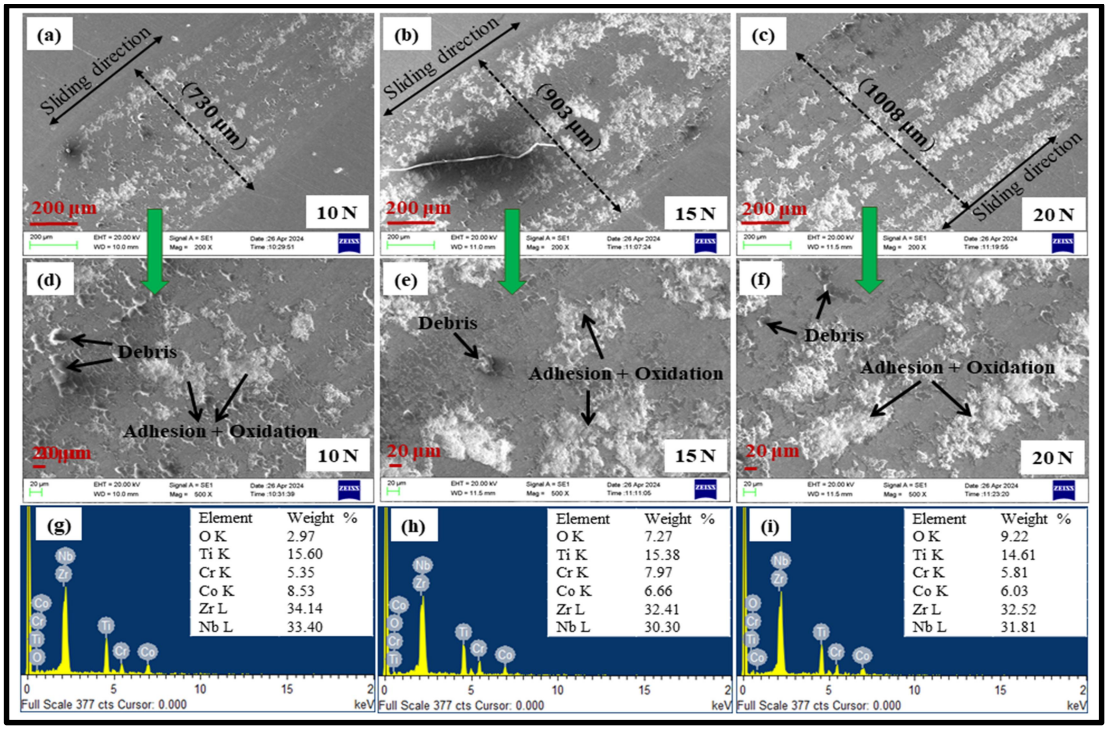

Fig. 7.14. SEM images and EDS analysis of the worn surface of Ti-$Co_{0.35}$-$Cr_{0.35}$-Nb-Zr sample at 10 N (a, d, g), 15 N (b, e, h), and 20 N (c, f, i) load after 7200 cycles in SBF.

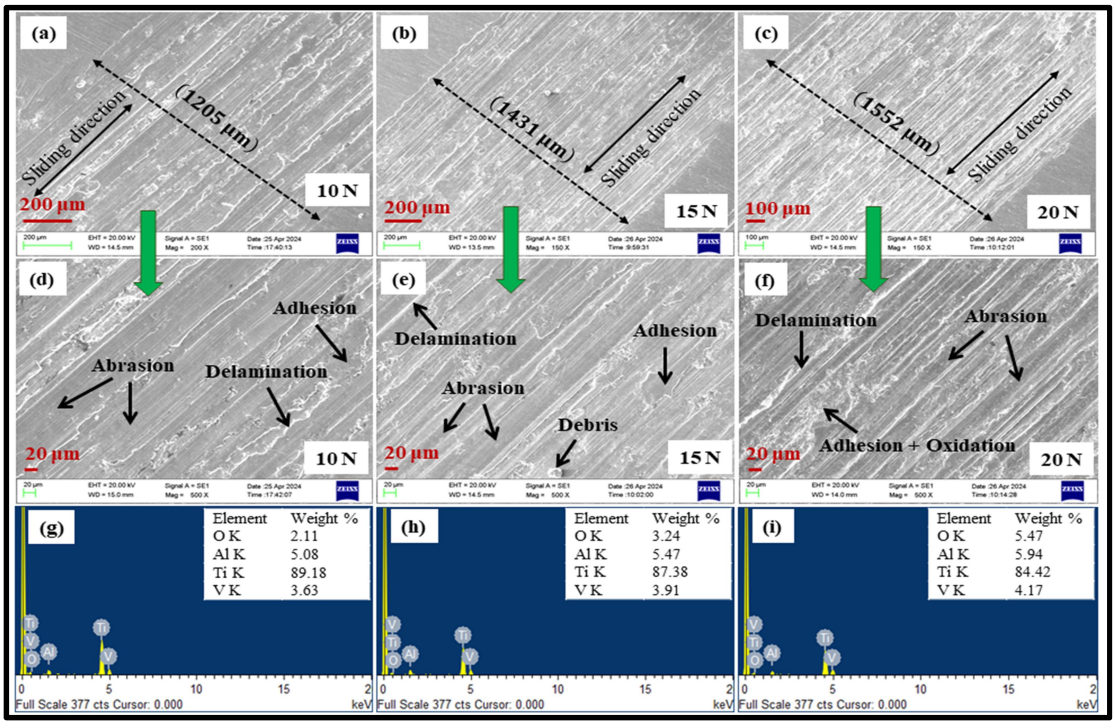

Fig. 7.15. SEM images and EDS analysis of the worn surface of Ti-6Al-4V sample at 10 N (a, d, g), 15 N (b, e, h), and 20 N (c, f, i) load after 7200 cycles in SBF.

7.4. Summary

The corrosion and wear analyses of the developed HEAs in SBF led to the following conclusions:

1. The developed HEAs exhibit more corrosion resistance and reduced corrosion rates as compared to Ti-6Al-4V alloy in SBF. Of the three developed HEAs, Ti-Nb-Ta-Cr-$Co_{0.2}$ shows to have the best corrosion resistance and the lowest corrosion rate.

2. Double protective layers were formed on the surface of HEAs during corrosion in SBF. The inner barrier layer is stronger than the outer porous layer.

3. The corroded surface of the HEAs reveals a pitting corrosion mechanism.

4. With the increase in load, the friction coefficient of the wear samples decreases while the wear volume and rate increases in the presence of SBF.

5. The wear-worn surfaces show adhesion, oxidation, abrasion, delamination, and wear debris.

6. The developed HEAs show lower worn wear rate than Ti-6Al-4V alloy in SBF, thus suitable for implant applications.